Low-energy Ar+ ion induced angularly resolved Al(100) and Al(110) sputtering measurements

P. C. Smith and D. N. Ruzic

Related Articles

Probe current distribution characterization technique for focused ion beam
J. Vac. Sci. Technol. B 30, 06F606 (2012)

From sponge to dot arrays on (100) Ge by increasing the energy of ion impacts
J. Vac. Sci. Technol. B 30, 06FF12 (2012)

New method of calculating adsorption and scattering for Xe-Pt(111) using Direct Simulation Monte Carlo techniques
J. Vac. Sci. Technol. A 30, 061401 (2012)

Current–voltage–time characteristics of the reactive Ar/O2 high power impulse magnetron sputtering discharge
J. Vac. Sci. Technol. A 30, 050601 (2012)

Influence of magnetic ordering on the elastic properties of PdFe3N
J. Vac. Sci. Technol. A 30, 030602 (2012)

Additional information on J. Vac. Sci. Technol. A

Journal Homepage: http://avspublications.org/jvsta

Journal Information: http://avspublications.org/jvsta/about/about_the_journal

Top downloads: http://avspublications.org/jvsta/top_20_most_downloaded

Information for Authors: http://avspublications.org/jvsta/authors/information_for_contributors

Low-energy Ar$^+$ ion induced angularly resolved Al(100) and Al(110) sputtering measurements

P. C. Smith[a) and D. N. Ruzic[b)

Department of Nuclear, Plasma, and Radiological Engineering, University of Illinois at Urbana-Campaign, Urbana, Illinois 61801

An apparatus and analysis method to obtain both the angular distribution of sputtered atoms and the total sputtering yield for materials of interest to physical vapor deposition (PVD) has been created. Total yield is determined by collecting the sputtered material on a quartz crystal oscillator (QCO) microbalance. The sputtered material is also collected on a pyrolytic graphite witness plate. By mapping the concentrations of the sputtered material on this plate, both polar and azimuthal angular distributions of the sputtered material can be determined. Utilizing this setup, data have been obtained for (200–500 eV) Ar$^+$ normally incident on polycrystalline aluminum sputtering targets with strong (100) and (110) crystallographic orientations. The overall yields of these samples compare well to the available data as well as empirical formulas. Crystallographic effects in the angular distributions are clearly seen. The Al(100) sample shows 12% enhanced sputtering along the $\langle 110 \rangle$ direction at all energies. © *1999 American Vacuum Society.* [S0734-2101(99)02606-8]

I. INTRODUCTION

In the design of most plasma vapor deposition (PVD) systems, the metal flux from the target is assumed to be emitted in a cosine angular distribution. Tool manufacturers even specify that target manufacturers must produce cosine-emitting targets. A PVD tool based on a target with a peaked flux profile could be beneficial for filling high aspect ratio features or reducing the clogging of collimators, but the magnitude and existence of such a profile has to be determined before such a tool would be designed.

Effects due to crystal orientation in real world sputtering devices have long been debated due to the difficulty in measuring their effects. That there are crystal effects is clear. Wehner observed in 1955 that sputtered particles from single-crystal targets (Ag, Cu, Ni, Fe, Ge, and W) due to Hg ion impact ($E < 400$ eV) exhibited maxima along the close-packed directions.[1,2] These maxima have since become known as ''Wehner spots.'' Since this discovery, numerous measurements over five orders of magnitude of projectile energy have clearly established this effect as a general effect of the irradiation of a crystalline solid.[3] The question then is whether the crystalline effects observed in these experiments can be extended to real sputtering devices. The surface of a sputtering target is made rough under the ion bombardment, and computer simulations indicate that a large fraction (90–95%) of the sputtered particles originate in the top layer.[4] Conversely as Betz has noted: ''The fact that these structures (Wehner spots) are observed at high fluences proves that at least for metals the regular lattice structure of the target recovers fast enough before the next particle hits near to the previous impact point.''[5] The question then is to what extent the bulk crystallinity can affect the sputtering process on a rough surface?

The closest research in the literature is studies of the crystallographic effects in secondary ion mass spectroscopy (SIMS). For example, the Al$^+$ distribution from lithium-doped Al(111) and Al(100) surfaces due to 4 keV Ar$^+$ was studied and maxima along the $\langle 110 \rangle$ direction were clearly observed.[6] Okada studied N$_2^+$, N$^+$, and Ne$^+$ in the energy range of 50–200 eV incident on Al(110) and Al(111).[7] Unfortunately, only angles of incidence of 45° and 60° were considered and data were taken only at a single azimuthal angle. Although some evidence of enhanced sputtering in the $\langle 110 \rangle$ direction is suggested, the data are inconclusive. A study was conducted by Szymczak on Au(111) (also fcc) with He$^+$, Ne$^+$, and Xe$^+$ ions with energies ranging from 100 to 270 keV.[8] In the case of 400 and 15 keV Xe$^+$ ions, enhanced sputtering along the $\langle 110 \rangle$ direction is obvious in both cases. The lower energy case shows features due to enhanced sputtering along the $\langle 100 \rangle$ direction as well, though these features are of a lower magnitude than those corresponding to the close-packed $\langle 110 \rangle$ direction. These SIMS studies do not directly observe the sputtered particles. Ionization efficiency can also exhibit crystallographic effects with single crystal targets. Additionally, the surfaces involved in those studies were highly polished samples and do not reflect conditions in a sputtering device.

This Ar$^+$ on Al work was motivated by a research relationship with TOSOH SMD, so it is not surprising that the most closely related papers are articles published by TOSOH researchers. In 1987 Wickersham conducted a study of Al film uniformities.[9] Utilizing conical targets with various crystallographic orientations, a 10% improvement in the film uniformity was demonstrated by simulation and experiment. In 1995 Bailey conducted a series of experiments on Al(100) and Al(110) samples.[10] A magnetron with rotating 50 mm target samples was operated and the sputtered flux was collected on a mylar film over polar angles of 0°–65°. The

---

[a)Current address: INTEL Corp., Hillsboro, OR.
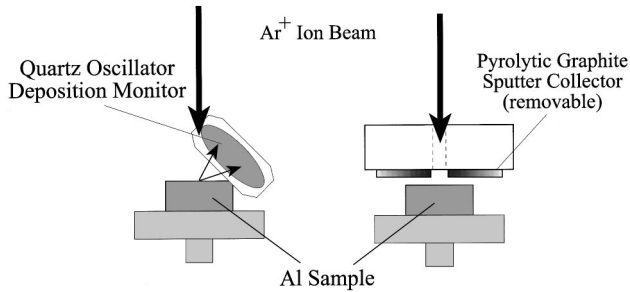[b)Electronic mail: druzic@uiuc.edu

FIG. 1. Detail of sputter data collection apparatus. Ar$^+$ normally incident on Al.

angular distribution was then inferred from optical transmission measurements on the mylar film.

In this experiment, we analyzed samples from actual Al-1%Si-0.5%Cu TOSOH SMD sputtering targets highly ordered in the (100) or (110) direction demonstrate and quantify the effect of crystallographic orientation on the angular distribution of the sputtered material. The apparatus and method allows for *in situ* sputter cleaning of the aluminum samples with an Ar$^+$ plasma prior to the determination of their angular-resolved sputtering yield. The absolute yield as well as the polar and azimuthal angular-resolved yield of the sputtered flux can be determined as a function of ion energy and angle of incidence for 10 eV to 1 keV ions.

II. EXPERIMENTAL APPARATUS

An ion beam is generated in a Colutron plasma based ion source.[11,12] It is then accelerated and focused at an energy of 700 eV by a three-element cylindrical electrostatic lens. The proper charge to mass ratio is then selected as the beam transits an $E \times B$ filter. The focused and species-selected beam passes next into the ultrahigh vacuum (UHV) chamber. The electrostatic repulsive force between the ions in the beam acts to spread the beam and decrease its intensity. The beam is transported at an energy of 700 eV so that the velocity of the ions is fairly high as they transit the system from source to target and the time of this interaction is minimized (10 ms). The deceleration of the beam to the desired energy and final focus is therefore performed as close to the target as possible. The deceleration is accomplished by a five-element cylindrical electrostatic lens that was modeled with the SIMION 3D[13] program. After transiting the decelerator, an electrostatic filter removes the neutral component from the beam immediately prior to the beam striking the target by jogging the ion path onto a parallel but unobstructed trajectory.

A schematic of the data collection apparatus is shown in Fig. 1. The target is fixed. Once the beam is focused, it will continue to strike the same grain of the target during the entire experiment. The witness plate is a grade ZYH pyrolytic graphite monochromator manufactured by Advanced Ceramics Corporation and is a 12 mm by 12 mm square. Pyrolytic graphite was chosen as collector for two reasons. First, being highly planar, the graphite readily formed extremely flat surfaces. By carefully applying a piece of ordinary scotch tape to the surface, a new layer can easily be cleaved when the tape is removed. Auger analysis of the witness plates after this cleaving but without any deposited films showed them to be remarkably free of contaminants. No other elemental lines are in evidence on the scan. This includes the often difficult to avoid oxygen line. The second reason for choosing pyrolytic graphite is that the Auger line of carbon (275 eV) is very distinct from the O (510 eV) and Al (68 eV) lines that were of interest in this study. After the target has been sputtered, the witness plate is removed from the vacuum and transferred to a PHI 660 Auger Spectrometer. The surface concentrations of Al are then determined to obtain angular distribution data.

Determining an exact angular distribution of sputtered material from a planar collector is impossible. Schulz and Sizman[14] show that the spread in the polar ejection angle close to a specific orientation direction, θ_0, makes it impossible to measure θ_0 unless a cylindrical or spherical collector plate is used. However, the azimuthal angle is not affected. If the emission pattern has fourfold symmetry, spots at those four angles will still be seen whether the collector is a plane, cylinder, or sphere. Since a planar collector is used here, the reported polar ejection angle is only accurate if there was no spread in emission from the target. Given a spread for the directed component, the reported polar angle may be too high by up to 15°. The reported relationship of the azimuthal peaks is valid.

Also shown in Fig. 1 is the arrangement of the quartz crystal oscillator. Although both the witness plate and the quartz crystal oscillator are mounted on the manipulator, the measurements are not simultaneous. The witness plate measurement is made and is immediately followed by the quartz crystal oscillator. It is difficult to determine the total sputtering yield from the witness plate data alone due to difficulties in modeling the surface film as well as issues of reflection and resputtering. Fortunately, these effects affect the witness plate nearly uniformly so that the areal densities obtained can be accurately compared to one another to obtain relative angular data. A quartz crystal oscillator microbalance was incorporated into the apparatus to allow for an independent measure of the total sputtering yield. The value obtained from this microbalance is then used to scale the distribution from the witness plate so that when integrated, it gives the proper total yield.[15]

III. DATA ANALYSIS

A. Areal density of sputtered material on the witness plane

The differential of intensity from a pure sample of material A (like the carbon of the witness plate) would be:[16]

$$dI_A = \kappa' S'_A N_A \exp\left(-\frac{x}{\lambda_A^A \cos(\phi)} \right) dV, \qquad (1)$$

where dI_A is the intensity of Auger electron spectroscopy (AES) peak of material A from element dV, κ' is a constant dependent upon the detection efficiency and x-ray flux,

properties of the instrument alone, S'_A is a constant dependent upon the Auger production efficiency and electron mean free paths, properties of material A alone, N_A is the atom density of material A, x is the distance below surface at which the Auger electron originates, λ_A^β is the mean free path of emitted electron of energy corresponding to the peak associated with element A traveling through material β [in Eq. (1), $\beta = A$], and ϕ is the angle of the electron detector with respect to the surface normal ($\phi = 0°$ for our experiment.)

In areas where the deposited Al layer is several monolayers, we must account for the shielding of the signal originating in the underlying layer (material A) by the deposited film (material B). Adding this shielding term, and noting that the cosine term is one, the equation becomes

$$dI_A = \kappa' S'_A N_A \exp\left(-\frac{x}{\lambda_A^A}\right) \exp\left(-\frac{t}{\lambda_A^B}\right) dV, \qquad (2)$$

where t is the thickness of the material B layer. We set $dV = dA\,dx$ and integrate though the volume of the sample.

$$I_A = \int_\infty^0 \kappa' S'_A N_A \exp\left(-\frac{x}{\lambda_A^A}\right) \exp\left(-\frac{t}{\lambda_B^A}\right) \Delta A\,dx. \qquad (3)$$

Since the area illuminated by the electron beam (ΔA) will be the same for all Auger electrons produced we can absorb ΔA into κ such that $\kappa = \kappa' \Delta A$. Integrating we obtain

$$I_A = \kappa S'_A N_A \lambda_A^A \exp\left(-\frac{t}{\lambda_B^A}\right). \qquad (4)$$

Rather than determining absolute measurements of the mean free paths and the other material dependent parameters, signals from each element are compared and related to a standard material. These material specific parameters than are contained in the sensitivity factors ($S_A = S'_A \lambda_A^A$).

$$I_A = \kappa S_A N_A \exp\left(-\frac{t}{\lambda_B^A}\right). \qquad (5)$$

For the signal from material B, the one deposited near the surface of the witness plate, the derivative is similar but we integrate x from 0 to t rather than 0 to infinity. For this case, Eq. (5) become

$$I_B = \kappa S_B N_B \left[1 - \exp\left(-\frac{t}{\lambda_B^B}\right)\right]. \qquad (6)$$

A ratio of these equations is then taken.

$$\frac{I_A}{I_B} = \frac{S_A N_A}{S_B N_B} \frac{\exp(-t/\lambda_B^A)}{[1 - \exp(-t/\lambda_B^B)]}. \qquad (7)$$

The intensities I_A and I_B, are measured. All of the other terms in this equation can be readily looked up allowing t, the thickness of the deposited layer, to be calculated. This equation is transcendental and as such has no closed form solution, but it can be solved numerically for the individual data points using an iterative algorithm. Once t is known, this value is converted into an areal density n_B by the following:

$$n_B = t N_B. \qquad (8)$$

TABLE I. Total yield measurements for the Ar⁺ on Al system.

Energy	Al(100)	Al(110)
200 eV	0.259±0.039	0.376±0.056
300 eV	0.444±0.067	0.481±0.072
400 eV	0.645±0.097	0.753±0.113
500 eV	0.743±0.111	0.820±0.123

B. Expected areal density from VFTRIM 3D

Several computer simulation runs were performed with the code VFTRIM 3D to serve as a basis for comparison. This is a binary collision code using an amorphous bulk and a fractal surface. A thorough discussion of this code can be found in Ref. 17. Additional information is available in Ref. 18. The results of these runs provided the energy and angular distribution of the sputtered Al particles, their sticking coefficient to C as well as an estimate of the reflection of the neutralized Ar ion flux and its effect in resputtering the deposited Al film. They are provided in the results section.

C. Calculation of the total yield from the QCO

The ion current to the target is integrated and the thickness change on the QCO is observed. That thickness is converted to ''numbers of Al atoms,'' by assuming the material on the QCO is Al_2O_3. This composition is confirmed by deliberate addition of oxygen to the UHV chamber after exposure and observing no weight increase. The solid angle subtended by the QCO is calculated and corrections due to (1) cosine emission, (2) sticking coefficient, and (3) resputtering of Al from fast reflected Ar are all taken into account to find the total sputtering yield. Complete details can be found in an earlier paper using this technique to measure the sputtering of Be by D.[19]

IV. RESULTS

The total sputtering yield for the Ar⁺ on Al experiments are shown in Table I and plotted in Fig. 2. Also shown on this figure are the results of previous investigators,[20,21] and empirical formula due to Bohdansky,[22] and results from the VFTRIM 3D code.

Figure 3 shows a surface plot for the case of 500 eV Ar⁺. The surface plots give a good representation of the grid layout of the collection plate. The vertical axis shows the concentration of Al on the plate and two horizontal axes represent the position on the plate. Each data point then is a value representing the amount of material at an intersection of the grid as predicted by (a) VFTRIM 3D and determined by (b) experiment. These same data are presented in Figs. 4(a) and 4(b) in the form of a contour plot. The contour plot is a convenient way to note perturbations in the distribution. Areas where the contour lines are close together indicate areas where the distribution changes rapidly. There is no correlation between the contour spacing and the spacing of the data points on the collection plate.

If the VFTRIM data in the surface plot are scaled to give the same yield as the experimental data, the only difference
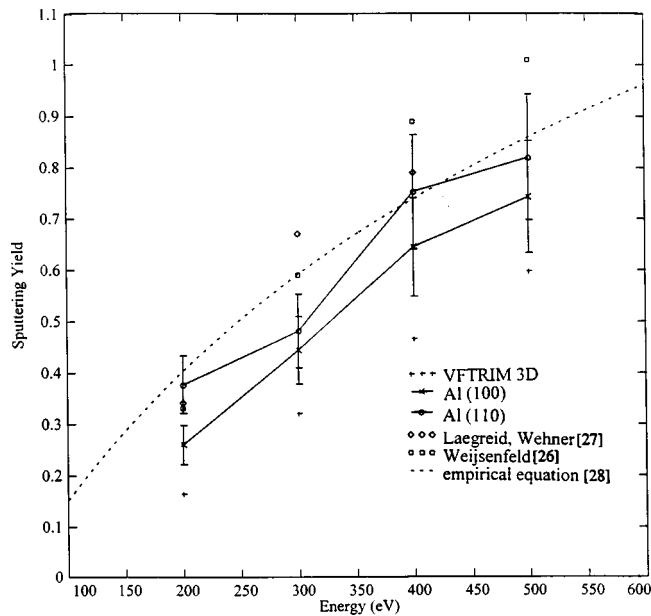
FIG. 2. Total yield measurements for the Ar$^+$ on Al system and comparisons to other work.

FIG. 4. Distribution of sputtered material from 500 eV Ar$^+$ on Al(100), (a) VFTRIM 3D, (b) experimental, (c) experimental minus VFTRIM-3D.

between the plots would be in the shape of the distribution. By subtracting this scaled VFTRIM plot from the experimental data and showing the results on a contour plot, the difference plot is obtained [Fig. 4(c)]. While peaks are evident in the distribution, they are most easily identified in this plot. Note that the two peaks are 90° away from each other in the azimuthal direction and are centered at polar angles of 45°.

Figure 5 shows the distribution of the sputtered flux versus the polar angle at azimuthal positions where a deviation from a cosine-like emission was noted. These plots contain data at the azimuthal angle corresponding to the emission direction and points within a few degrees of this angle. If there was no polar e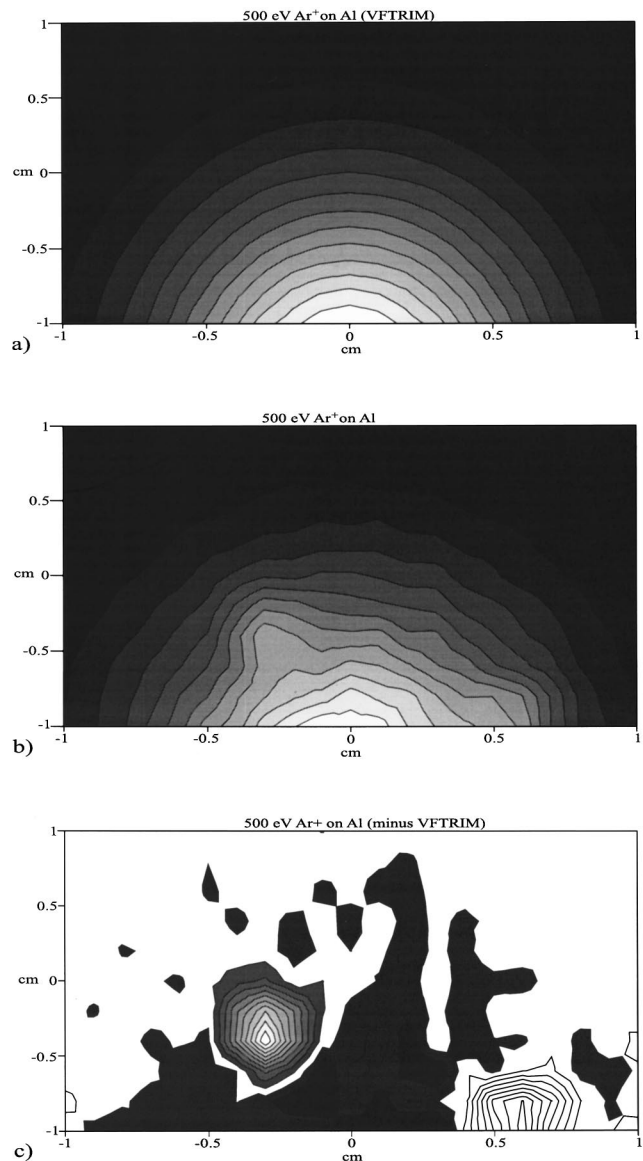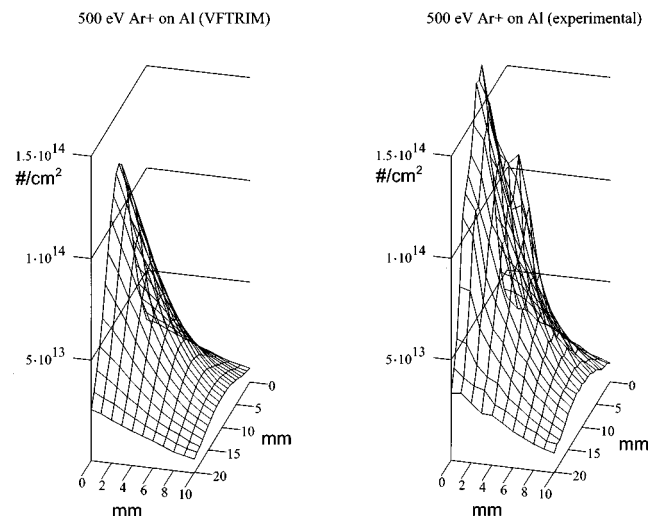jection angle spread in the enhanced emission portion of the spectra, this plot suggests that the enhanced sputtering is occurring at the 45° polar angle position ⟨110⟩. Since the magnitude of the spread is unknown, the actual polar ejection angle could be smaller.

To quantify the magnitude of the directional sputtering the following ratio was taken:

$$\eta = \frac{N_{110} - N}{N}, \tag{9}$$

where η is the fraction of additional sputtered material due to preferential sputtering in the ⟨110⟩ direction, N_{110} is the total amount sputtered in the ⟨110⟩ direction and N is the amount normally sputtered in the ⟨110⟩ direction without crystal effects. Even if the specific polar angle is incorrect, η still gives a measure of the enhanced sputtering magnitude.
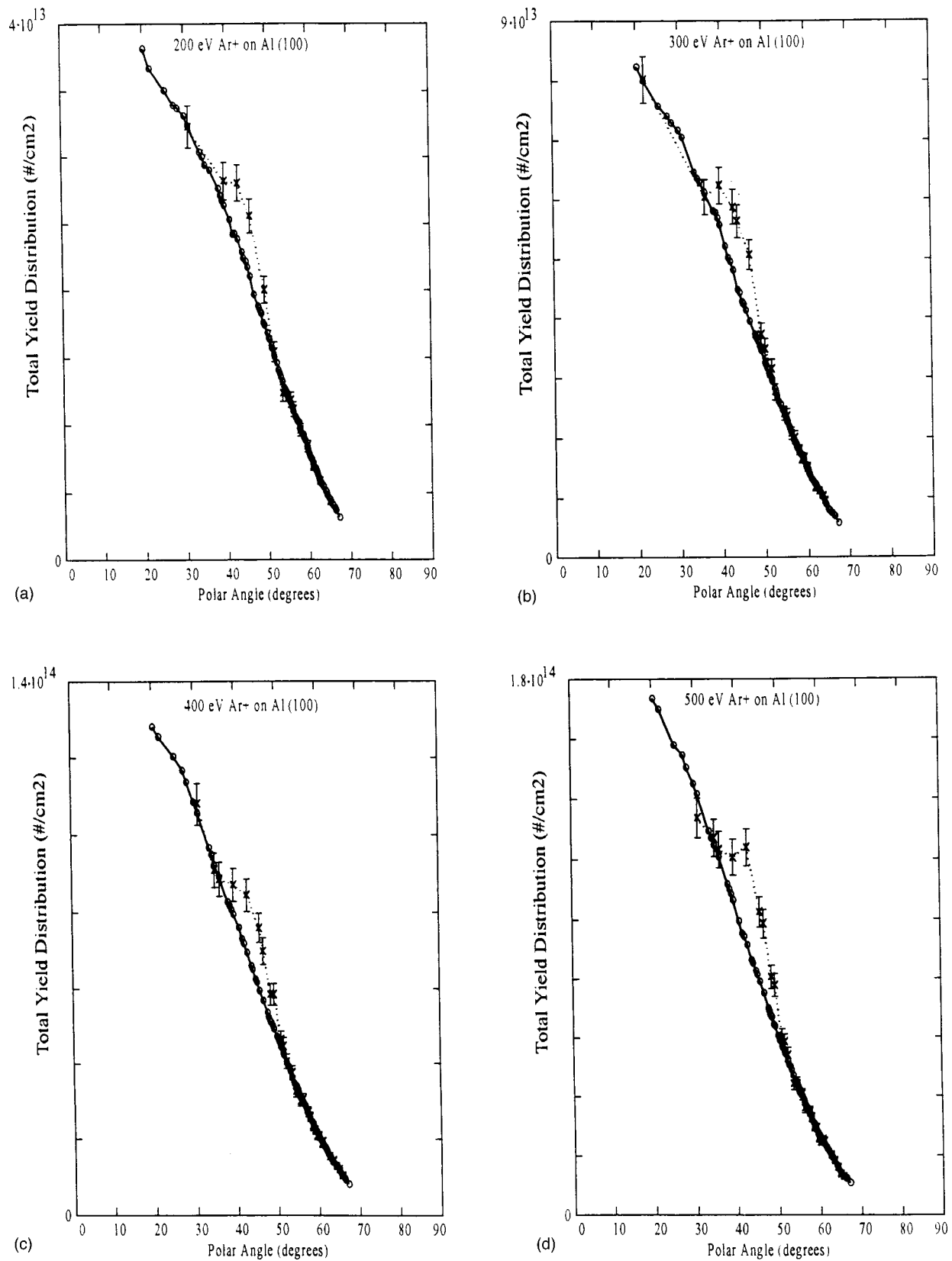

FIG. 3. Distribution of sputtered material from 500 eV Ar$^+$ on Al(100) (surface plot), (a) VFTRIM 3D, (b) experimental.

FIG. 5. Sputter distribution vs polar angle [Ar⁺ on Al(100)]. The experimental points are shown by crosses (×) with error bars. The points representing no azimuthal asymmetry and taken from the VFTRIM 3D simulation are shown as open circles (○). (a) 200 eV, (b) 300 eV, (c) 400 eV, (d) 500 eV.

TABLE II. Quantification of crystal effect.

Energy	η	$\Delta\Phi$
200 eV	12.9%	$\pm2.5°$
300 eV	11.4%	$\pm4.0°$
400 eV	13.4%	$\pm5.0°$
500 eV	11.2%	$\pm5.0°$

The results of this calculation for the Al(100) sample are shown in Table II along with the size of the azimuthal angle used to select points.

To determine how close the sputtered flux comes to a cosine distribution at the majority of azimuthal angles, Table III shows the parameter n when the data are fitted to a $\cos^n(\Theta)$ distribution.

V. DISCUSSION

The total sputtering yield for Ar$^+$ on Al experiments from the literature are plotted in Fig. 2 along with the experiment and simulation. The total yields in the Al(100) and (110) cases are very similar with the (100) case being slightly lower. The data from Weijsenfeld[26] and Laegreid/Wehner[27] are in very good agreement. The VFTRIM 3D yields are low. The surface binding energy can be adjusted to bring this up to the other values, but this is usually taken to be the sublimation energy and the only justification to lower this value would be to match the data. Since such pains were taken to make the simulation and experimental values completely independent, the simulation values were not altered. More work realistically changing the binding energy of the surface model in the code will be published soon.

The experimentally determined angular distributions show some very interesting characteristics. Though the Al(100) sample is not a single crystal, the size of the grains and the data are consistent with hitting only one (100) grain. From the (100) plane the family of close-packed $\langle110\rangle$ directions is expected to radiate at a polar angle of 45° and are separated from one another by 90° in azimuthal angle. The effects in the distribution of preferred sputtering along the $\langle110\rangle$ directions are clearly evident, though the exact 45 degree angle cannot be confirmed due to the planar collector plate.

The $\langle110\rangle$ direction for the Al(110) sample is normal to the sample. Since the beam itself was normally incident, no measurements could be taken of the distribution at this angle. It is not surprising then that the Al(110) samples did not exhibit any notable preferential sputtering along the observable directions. The surface plots for the Al(110) case only show the expected experimental scatter.

The magnitude of the effect of the enhanced $\langle110\rangle$ sputtering (about 12%) was roughly the same over the various energies, however, the width of the peak was broader for the higher energies. As in the case of D$^+$ on Be,[23] the distributions are undercosine approaching cosine at the higher energies. This is in agreement with computer simulation and previous experiments where undercosine behavior is noted for lower energies and overcosine behavior is observed for energies in the keV range.[24–27]

TABLE III. Fitting to a $\cos^n(\Theta)$ distribution.

Energy	n
200 eV	0.83 ± 0.15
300 eV	0.91 ± 0.16
400 eV	0.95 ± 0.15
500 eV	1.01 ± 0.15

[1] G. K. Wehner, J. Appl. Phys. **26**, 1056 (1955).
[2] G. K. Wehner, Phys. Rev. **102**, 690 (1956).
[3] W. O. Hofer, in *Sputtering by Particle Bombardment III*, edited by R. Behrisch and K. Wittmaack (Springer, Berlin, 1991).
[4] G. Betz and W. Husinsky, Nucl. Instrum. Methods Phys. Res. B **102**, 281 (1995).
[5] G. Betz and K. Wien, Int. J. Mass Spectrom. Ion Processes **140**, (1994).
[6] A. Johansen, E. Johnson, L. Sarholt Kristensen, S. Steenstrup, H. Anderson, V. M. Buhanov, V. S. Chernysh, I. N. Ivanov, and K. F. Minnebaev, Nucl. Instrum. Methods Phys. Res. B **61**, 21 (1991).
[7] M. Okada and Y. Murata, Surf. Sci. **291**, 451 (1993).
[8] W. Szymczak and K. Wittmaack, Nucl. Instrum. Methods Phys. Res. B **82**, 220 (1993).
[9] C. E. Wickersham, J. Vac. Sci. Technol. A **5**, 1755 (1987).
[10] R. S. Bailey and N. C. Hill, Proc. SPIE **2637**, 56 (1995).
[11] L. Wahlin, Nucl. Instrum. Methods **27**, 55 (1964).
[12] M. Menzinger and L. Wahlin, Rev. Sci. Instrum. **40**, 102 (1969).
[13] D. A. Dahl, SIMION3D version 6.0 (Lockheed Martin Idaho Technologies, Idaho National Engineering Laboratory, 1990).
[14] F. Schulz and R. Sizmann, Philos. Mag. **18**, 269 (1968).
[15] G. Z. Sauerbrey, Z. Phys. **155**, 206 (1959).
[16] M. P. Seah, in *Practical Surface Analysis Vol. 1, Auger and X-ray Photoelectron Spectroscopy*, edited by D. Briggs and M. P. Seah (Wiley, Chichester, 1990).
[17] R. B. Turkot, Ph.D. thesis, University of Illinois, 1996.
[18] M. A. Shaheen and D. N. Ruzic, J. Vac. Sci. Technol. A **11**, 3085 (1993).
[19] D. N. Ruzic, P. C. Smith, and R. B. Turkot, Jr., J. Nucl. Mater. **241**, 1170 (1997).
[20] C. H..Weijsenfeld, Philips Res. Rep. **2**, (1967).
[21] N. Laegreid and G. K. Wehner, J. Appl. Phys. **32**, 365 (1961).
[22] J. Bohdansky, Nucl. Instrum. Methods Phys. Res. B **2**, 587 (1984).
[23] P. C. Smith and D. N. Ruzic, Nucl. Fusion **38**, 673 (1998).
[24] Y. Yamamura and K. Muraoka, Nucl. Instrum. Methods Phys. Res. B **42**, 175 (1989).
[25] H. H. Andersen, B. Stenum, T. Sorensen, and H. J. Whitlow, Nucl. Instrum. Methods Phys. Res. B **6**, 459 (1985).
[26] F. R. Vossen, J. Vac. Sci. Technol. **1**, 875 (1974).
[27] Y. Matsuda, Y. Yamamura, Y. Ueda, K. Uchino, K. Muraoka, M. Maeda, and M. Akazaki, Jpn. J. Appl. Phys., Part 1 **24**, 8 (1986).